Environmental Fluid Mechanics (2020) 20:1075–1100
https://doi.org/10.1007/s10652-020-09742-w

ORIGINAL ARTICLE

Singular air entrapment at vertical and horizontal supported jets: plunging jets versus hydraulic jumps

Livia Müller[1] · **Hubert Chanson**[1]

Received: 1 December 2019 / Accepted: 3 April 2020 / Published online: 21 April 2020
© Springer Nature B.V. 2020

Abstract
In plunging jets and at hydraulic jumps, large amounts of air bubbles are entrained at the impingement of the liquid jet into the receiving body. Air is entrapped and advected into a turbulent shear layer with strong interactions between the air bubble advection process and momentum shear flow. In this new physical study, air–water flow measurements were systematically repeated with identical inflow length, inflow depth and inflow velocity in a vertical supported jet (PJ) and a horizontal hydraulic jump (HJ). Detailed measurements were conducted with the same instrumentation. Both similarities and differences were observed between the two multiphase gas–liquid shear flows. Visual observations showed a key difference in the outer region, with a buoyancy-driven flow in the plunging jet with negligible void fraction, versus a strong recirculation motion with uncontrolled interfacial aeration in the hydraulic jump. Differences were also observed at the impingement perimeter, in terms of fluctuation frequencies and amplitudes, for identical inflow conditions. Both flow conditions yielded intense local singular air entrainment and close results were observed in terms of void fraction, bubble count rate, bubble chord sizes and interfacial area in the shear layer, in both the plunging jet and hydraulic jump. The transfer of momentum between impinging jet and receiving water, as well as the effect of buoyancy, were however affected by the flow geometry.

Keywords Air bubble entrainment · Plunging jets · Hydraulic jumps · Physical modelling · Singular aeration

1 Introduction

With the very different fluid specific weight, the free-surface is typically a sharp interface between air and water. There are however situations leading to strong mixing of air and water, a phenomenon called air bubble entrainment or self-aeration [27, 34]. Both plunging jets and hydraulic jumps are examples of local air entrainment and may commonly occur in hydraulic, chemical, industrial and natural applications [9]. A plunging jet is defined as a water jet impinging a receiving pool of water. Large amounts of air bubbles are entrained

✉ Hubert Chanson
h.chanson@uq.edu.au

[1] School of Civil Engineering, The University of Queensland, Brisbane, QLD 4072, Australia

at the impingement of the liquid jet and receiving body [4, 16]. Entrapped air bubbles are advected into a turbulent shear layer with strong interactions between the air advection process and momentum shear flow [14, 15, 20, 31]. Considering the simple case of a vertical supported jet, a free shear layer develops immediately downstream of the jet impact, and the impingement perimeter is a line source of vorticity and air bubbles. A related shear flow situation is the horizontal hydraulic jump. It is characterised by a transition from supercritical flow to a subcritical flow [1]. Strong energy dissipation, air entrainment and large-scale turbulence take place [21, 24, 33]. Applications of hydraulic jumps include stilling basins of a dam, weirs and aeration structures for oxygen balance of a river system [27]. Analogies between a shockwave from a supernova explosion and a circular hydraulic jump have also been proposed by Foglizzo et al. [19].

An earlier study showed some analogy in terms of void fraction distributions between hydraulic jumps and plunging jets, albeit without identical inflow conditions and a limited data set [7]. Herein new air–water flow measurements were repeated with identical inflow depth and velocity in a vertical supported jet and a horizontal hydraulic jump. The new two-phase flow measurements presented both similarities and differences between the two gas–liquid shear flow configurations. The results are discussed in terms of the two-phase flow properties.

2 Physical experiments and instrumentation

2.1 Experimental facilities

The two-phase flow measurements were performed in two distinct large-size experimental channels, with the same multiphase flow instrumentation and identical inflow conditions for all series of experiments.

The vertical plunging jet experiments were conducted in a two-dimensional vertical supported jet channel, previously used by Bertola et al. [2, 3] (Fig. 1a). The receiving tank was 1.5 m deep, 1.0 m wide and 2.5 m long, with glass walls (Fig. 2a). The jet nozzle was 0.27 m wide (B = 0.27 m) and 0.012 m thick, followed by a 0.35 m long jet support, at 89º from the horizontal to prevent flow separation. The horizontal supported jet facility was a 3.2 m long 0.5 m wide (B = 0.5 m) hydraulic jump flume (Fig. 1b). The channel invert was made out of HDPE and the sidewalls were 3.2 m long glass panels (Fig. 2b). The flume was horizontal and the inflow was delivered through an adjustable vertical rounded gate. The downstream water conditions were controlled by an overshoot gate located at the downstream end.

Both facilities were supplied with a constant head water reticulation system, enabling a perfectly constant water discharge during the entire experiments. The same instrumentation and inflow conditions were used for both series of experiments.

2.2 Instrumentation

The clear-water jet thickness was measured using rail-mounted pointer gauges, with an accuracy of ± 0.5 mm. The water discharge was measured with a Venturi meter designed based upon British Standards and calibrated on site, with an expected error of less than 2%. A Dwyer® 166 Series Prandtl-Pitot tube was used to record clear-water velocity. The tube diameter was 3.18 mm with a hemispherical total pressure tapping at the tip

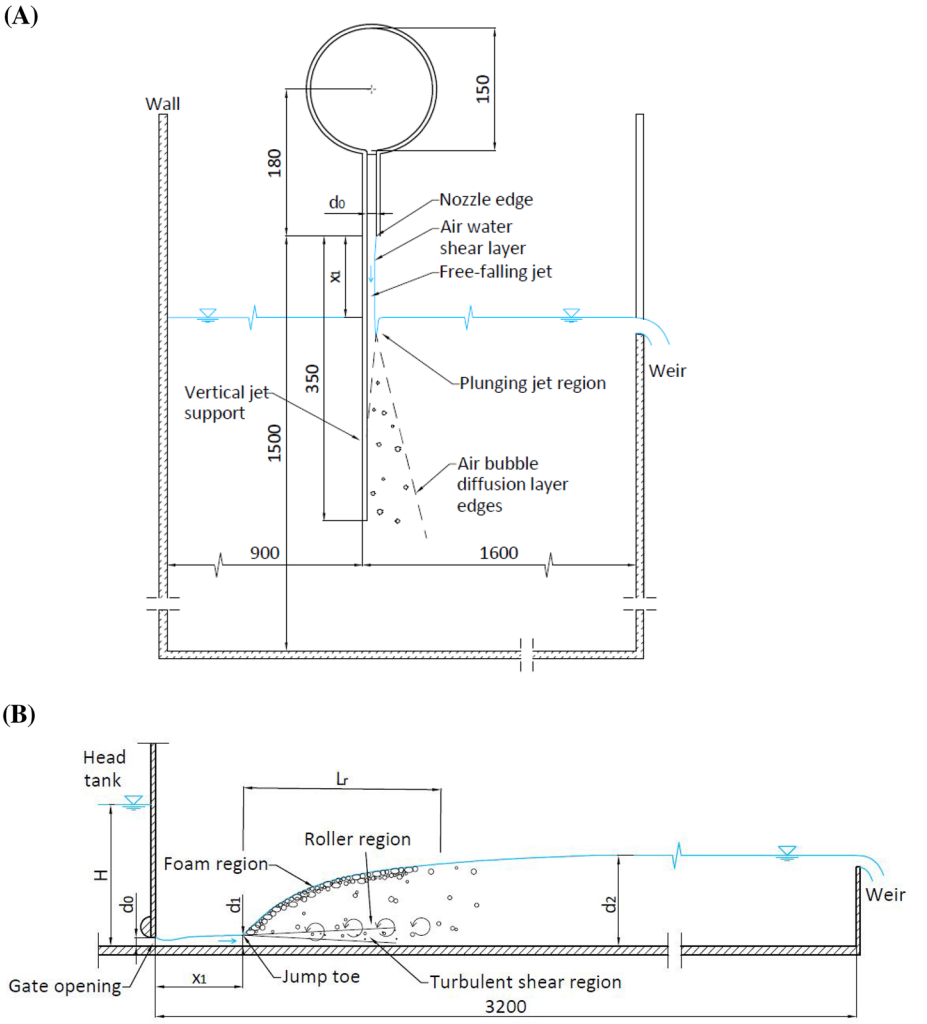

Fig. 1 Definition sketches of the vertical supported plunging jet and horizontal hydraulic jump channels. **a** Vertical supported plunging jet channel, **b** horizontal hydraulic jump channel

(⌀ 1.18 mm) and eight static pressure holes (⌀ 0.4 mm) equally spaced, located 27 mm behind the tip. Calibration was not needed because of the ASHRAE tip design.

The air–water flow properties were recorded using two dual-tip phase-detection probes. Each dual-tip probe was equipped with two needle sensors developed at the University of Queensland. Each needle sensor consisted of an inner electrode insulated from the outer needle (ID = 0.5 mm). One probe had an inner electrode made out of silver wire (Ø = 0.25 mm), while the other used a stainless steel acupuncture needle (Ø = 0.18 mm). Each dual-tip probe was manufactured with two identical sensors separated transversally by $\Delta z = 2$ mm and 2.3 mm, with the leading and trailing sensors were separated longitudinally by $\Delta x = 4$ mm to 6 mm. The probe sensors were simultaneously

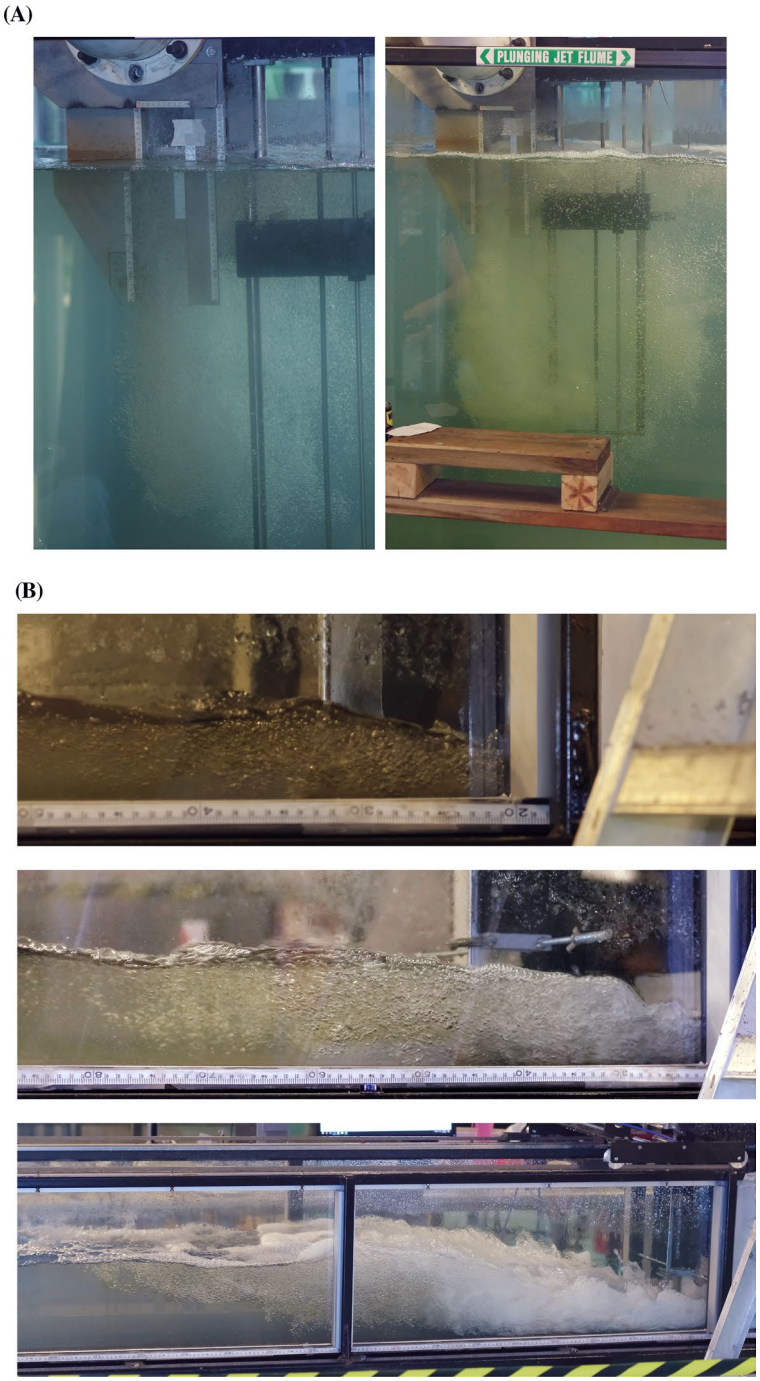

Fig. 2 Photographic observations. **a** Vertical supported plunging jet channel: (Left) $V_1 = 2.46$ m/s; (Right) $V_1 = 4.5$ m/s, **b** horizontal hydraulic jump channel: (Top) $V_1 = 1.79$ m/s; (Middle) $V_1 = 2.46$ m/s (Bottom) $V_1 = 4.5$ m/s—Flow direction from right to left

excited by an air bubble detector electronics (Ref. UQ82.518) with a response time less than 10 μs. The sampling rate was 20 kHz per sensor for 90 s for all probes.

Flow visualisations were conducted with two cameras: a Sony™ Xperia XA1 Ultra camera with a frame rate of 30 fps and a resolution of 1920×1080 pixels, and a Casio™ EX-10 Exilim operating at 30 fps or 120 fps with a resolution of 640×480 pixels. For the advection speed of the vortices as well as for estimating the toe fluctuation frequency, the videos were analysed manually to guarantee maximum reliability of the data. For the impingement perimeter characteristics, the video movies were processed with Matlab™ using 1200 frames. Photographic observations were also undertaken with a dSLR camera Pentax™ K3 (Fig. 2).

2.3 Experimental flow conditions

The experiments were carried out for three different inflow conditions, with impact velocities $V_1 = 1.79$ m/s, 2.46 m/s and 4.5 m/s for both the plunging jet and hydraulic jump. The free jet length x_1 was also constant for all inflow velocities in both setups: $x_1 = 0.1$ m. The gate opening in the hydraulic jump was chosen in a manner to reproduce the same impingement conditions as in the plunging jet. The same impingement velocity V_1 and jet thickness d_1 were achieved, as well as the same impingement Froude and Reynolds numbers denoted Fr_1 and Re_1. Table 1 summarises the inflow conditions for the present study. Herein, the Froude, Reynolds and Morton numbers are defined as:

$$Fr_1 = \frac{V_1}{\sqrt{g\, d_1}} \tag{1}$$

$$Re_1 = \rho \frac{V_1\, d_1}{\mu} \tag{2}$$

$$Mo = \frac{g\, \mu^4}{\rho\, \sigma^3} \tag{3}$$

Table 1 Experimental flow conditions (Present study)

Apparatus	B	Q	d_o	x_1	d_1	V_1	Fr_1	Re1	Mo	d_2
	m	m^3/s	m	m	m	m/s				m
Plunging jet	0.27	0.0037	0.012	0.098	0.0076	1.79	6.56	1.37×10^4	2.54×10^{-11}	N/A
	0.27	0.0067	0.012	0.089	0.0101	2.46	7.80	2.48×10^4	2.54×10^{-11}	N/A
	0.27	0.0139	0.012	0.098	0.0114	4.5	13.45	5.14×10^4	2.54×10^{-11}	N/A
Hydraulic jump	0.5	0.0067	0.008	0.098	0.0077	1.79	6.52	1.37×10^4	2.54×10^{-11}	0.066
	0.5	0.0118	0.01	0.089	0.0101	2.46	7.80	2.48×10^4	2.54×10^{-11}	0.107
	0.5	0.0247	0.011	0.098	0.0112	4.5	13.55	5.14×10^4	2.54×10^{-11}	0.213

B: channel width; d_1: jet thickness at impingement; d_2: hydraulic jump conjugate depth; d_o: jet thickness at nozzle; Fr_1: jet Froude number at impingement; Mo: Morton number $Mo = g\times\mu^4/(\rho.\sigma^3)$; Q: water discharge; Re_1: jet Reynolds number at impingement; V_1 jet velocity at impingement; x_1: longitudinal distance from nozzle to impingement

with g the gravity acceleration, ρ and μ the density and dynamic viscosity of water respectively, and σ the surface tension of air and water.

3 Basic flow observations

3.1 Presentation

In a plunging jet, air entrapment takes place at the interface between the plunging jet and the receiving pool of water [17]. The impingement perimeter is a flow singularity and line source of vorticity and air bubble entrainment [9]. Downstream of the impingement point, two substantially different flow regions may be distinguished, as illustrated in Figs. 1a, 2a. These are the momentum shear layer, where viscous forces are dominant, and the outer region, where the movement of the air bubbles is mainly buoyancy-driven [30, 34]. In a hydraulic jump, the jump toe represents the impingement point of air entrainment [25]. Similar to the plunging jet, two flow regions are found downstream of the jump toe (Fig. 1b, 2b): the shear layer and the recirculation region above. The recirculation region is characterised by a negative velocity, in the opposite direction of the impinging flow. Importantly, in both the plunging jet and hydraulic jump, the developing shear layer does not coincide with the advective-diffusion layer of air.

Although both plunging jets and hydraulic jumps are examples of local air entrainment, there are some differences between the two flow situations. The four main differences are:

(a) *Wall jet analogy* An analogy between a hydraulic jump and a plane turbulent wall jet was first proposed by Rajaratnam [26]. The velocity profile in the shear layer of the hydraulic jump is very close to a wall jet pattern [12, 26].
(b) *Outer/recirculation region* An important difference is the recirculation movement in the upper flow region in the hydraulic jump. While the outer region is buoyancy-driven in the vertical plunging jet (Fig. 2a), the hydraulic jump shows an important recirculation motion in the upper part of the flow (Fig. 2b).
(c) *Buoyancy force direction* In regions outside the shear layer, the movement of the bubbles tends to be buoyancy driven. The buoyancy force always act in the opposite direction to the gravity force, leading to a 90° rotation between the flow direction and the direction of buoyancy force for the hydraulic jump and a 180° rotation for the plunging jet.
(d) *Interfacial air–water exchange* Both the plunging jet and the hydraulic jump are examples of local air entrainment at the impingement perimeter. In the hydraulic jump however, a large amount of un-controlled interfacial aeration and de-aeration are observed through the roller surface.

3.2 Advection of large coherent structures

In the developing shear layer, large-scale coherent structures are advected downstream and may grow through vortex pairing (Fig. 3). The roll-up of large eddies in the shear layer is not symmetric across the shear layer, favouring the entrainment of high-speed fluid (i.e. water herein) in the cores [6, 23]. The advection speed U_{eddy} of the large vortices was measured between their formation at the impingement point and the downstream flow region. Figure 4a, b present the probability density functions (PDF) of the advection speed of vortices in the

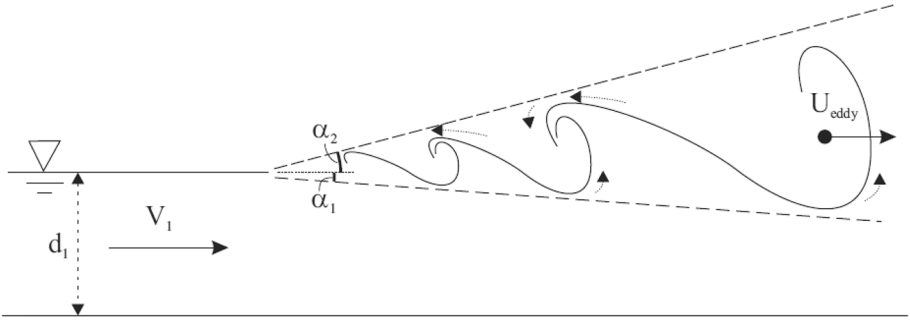

Fig. 3 Advection of large vortical structures in the developing shear layer

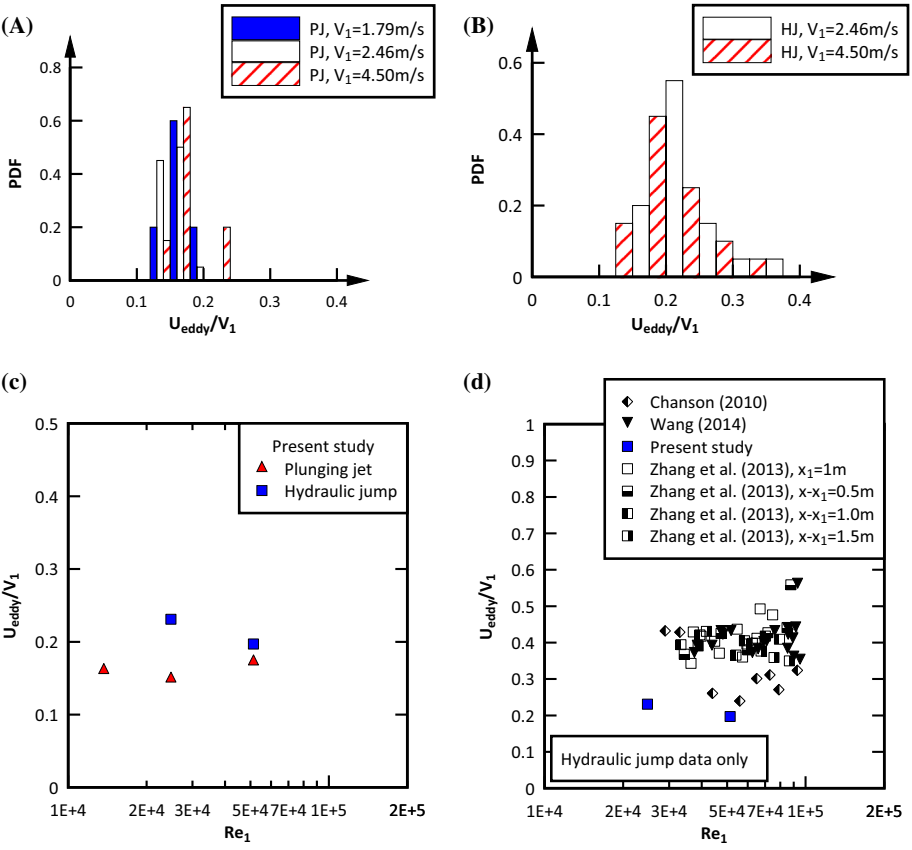

Fig. 4 Dimensionless advection speed U_{eddy}/V_1 of large vortices in turbulent shear region of vertical plunging jet and horizontal hydraulic jump, (**a**, Left) Probability distribution functions of dimensionless advection speed U_{eddy}/V_1 in the plunging jet, (**b**, Right) Probability distribution functions of dimensionless advection speed U_{eddy}/V_1 in the hydraulic jump, (**c**, Left) Dimensionless advection speed U_{eddy}/V_1 as a function of the inflow Reynolds number Re_1—Comparison between plunging jet and hydraulic jump (Present data), (**d**, Right) Dimensionless advection speed U_{eddy}/V_1 as a function of the inflow Reynolds number Re_1 in hydraulic jump—Comparison with literature data [11, 35, 32]

plunging jet and hydraulic jump respectively. In the plunging jet flow, the data were very close for all three inflow velocities, yielding $U_{eddy}/V_1 = 0.16$ in average. The advection speed of vortices in the hydraulic jump could not be recorded accurately for the smallest inflow velocity, $V_1 = 1.79$ m/s, because no defined large-scale motion could be identified as very little air was entrained at the roller toe. The data for the two highest inflow velocities yielded $U_{eddy}/V_1 = 0.21$ in average. Overall the advection speed of vortices was smaller in the plunging jet than in the hydraulic jump as illustrated in Fig. 4c.

The present hydraulic jump data are compared to the literature in Fig. 4d. The results suggested that the vortex advection speed in the present study was smaller than in previous studies, but still within the same order of magnitude. Importantly all data showed the dimensionless advection speed of vortices to be independent of the inflow Froude and Reynolds numbers (Fig. 4c, d).

A most interesting part of this investigation concerns the advection of large coherent structures, clearly visualised by the air entrapment in the eddy cores. As they are advected in the turbulent layer, the spacing between structures increased with increasing distance downstream, while the eddy diameter also increased as a result of vortex paring.

3.3 Impingement perimeter characteristics

All experiments were undertaken with a mean longitudinal distance between the nozzle and impingement location: $x_1 = 0.1$ m. Visual observations showed however that the impingement perimeter in the plunging jet and hydraulic jump constantly fluctuated about its mean position. Figure 5 illustrates typical instantaneous impingement perimeter data. In Fig. 5, the dashed area (i.e. $x < 0$) corresponds to the jet nozzle. Table 2 regroups some key findings.

In the plunging jet, the probability density function of the instantaneous impingement perimeter followed a quasi-normal distribution at all transverse locations, with the mode around the median value. In the hydraulic jump, a bimodal distribution of the instantaneous roller toe position was observed. Two peaks were recorded at $x/d_1 = 0$ and at the median value. The bi-modal distribution was due to the physical presence of the upstream gate, hindering the jump toe to move upstream past $x = 0$.

The experimental data showed that the impingement perimeter fluctuated with different frequencies and amplitudes, depending upon the inflow conditions and geometry. The impingement properties between plunging jet and hydraulic jump showed substantial differences under the same inflow conditions (x_1, V_1, d_1). Much larger longitudinal fluctuations of the impingement position were observed in the hydraulic jump compared to the plunging jet (Fig. 5). In average, the fluctuation amplitudes were one order of magnitude larger in the hydraulic jump. The impingement perimeter fluctuation frequencies were overall higher for the plunging jet than for the hydraulic jump (Table 2). Different frequencies were observed for all three inflow velocities in the plunging jet, whereas they were about the same in the hydraulic jump for all three inflow velocities.

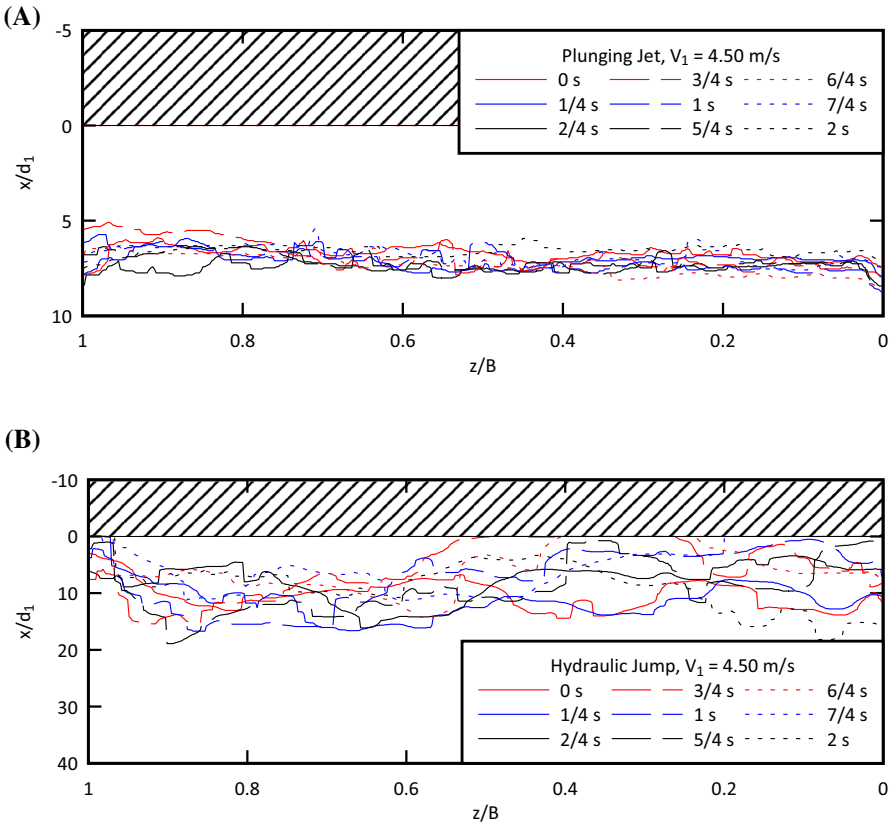

Fig. 5 Instantaneous impingement perimeter every 0.25 s for $V_1 = 4.50$ m/s in the plunging jet and hydraulic jump—Flow direction from top to bottom—Note the different vertical scales between Figs. 4a, c, **a** Plunging jet data—$x_1 = 0.1$ m, $x_1/d_1 = 8$, **b** Hydraulic jump data—$x_1 = 0.1$ m, $x_1/d_1 = 8.7$

Table 2 Fluctuation frequencies and maximum amplitudes of the impingement perimeter fluctuations in plunging jet and hydraulic jump

Inflow velocity V_1 (m/s)	Inflow Froude number Fr_1	Inflow Reynolds number Re_1	Fluctuation frequency f (Hz)		Maximum amplitude Δ (mm)		Strouhal number $St = \frac{f \times d_1}{V_1}$	
			PJ	HJ	PJ	HJ	PJ	HJ
1.79	6.5	1.37×10^4	5.1	2.7	2	30–40	0.0216	0.0116
2.46	7.8	2.48×10^4	2.2	2.7	3	40	0.0090	0.0111
4.50	13.5	5.14×10^4	1.7	2.7	10	60–80	0.0043	0.0068

HJ hydraulic jump, *PJ* plunging jet

4 Air–water flow properties

4.1 Void fraction and bubble count rate distributions

The turbulent shear region and the recirculation region were clearly evidenced in terms of the void fraction distributions. Figure 6 shows typical void fraction distribution for an inflow velocity $V_1 = 4.50$ m/s at two longitudinal locations.

In the plunging jet, the void fraction distributions followed a pseudo-Gaussian shape, reaching a maximum C_{max} in the advective diffusion layer of air. Away from the support,

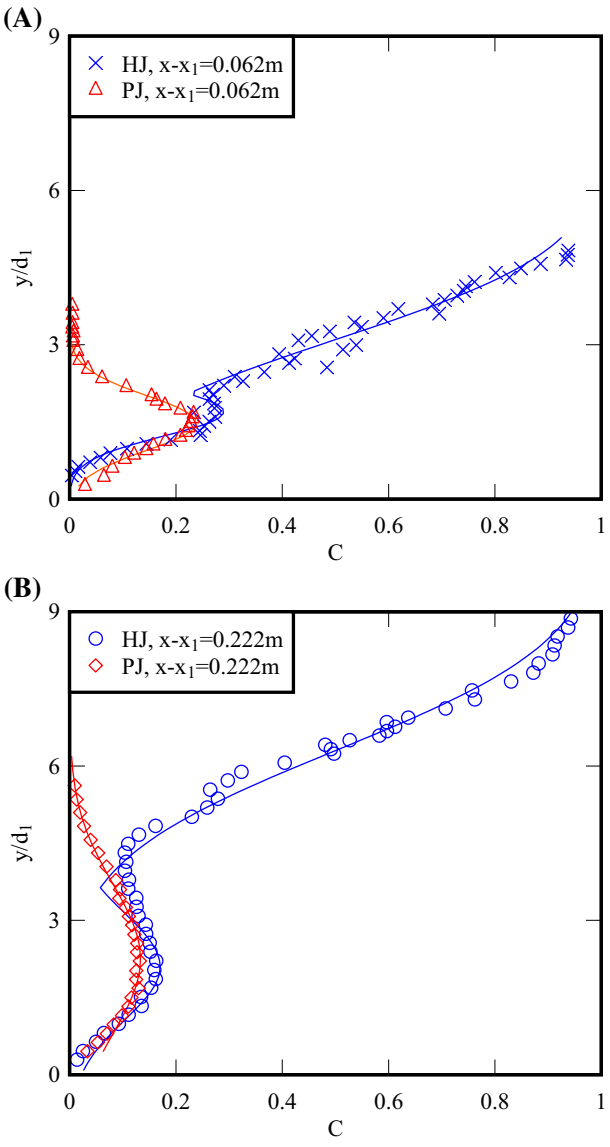

Fig. 6 Dimensionless distributions of time -averaged void fraction in the vertical plunging jet and horizontal hydraulic jump for $V_1 = 4.5$ m/s—Comparison with Eqs. (4) (turbulent shear layer) and (5) (recirculation region), **a** $(x\text{-}x_1)/d_1 = 5.4$, **b** $(x\text{-}x_1)/d_1 = 19.5$

the motion of bubbles was buoyancy driven. The peak in void fraction decreased with increasing distance from the impingement point ($x-x_1$), while the bell shape widened. The void fraction data compared favourably with an analytical solution of the air bubble advective diffusion [14]:

$$C = \frac{\frac{Q_{air}}{Q}}{\sqrt{4\pi D^{\#} \frac{x-x_1}{Y_{Cmax}}}} \cdot \left[\exp\left(-\frac{\left(\frac{y}{Y_{Cmax}} - 1\right)^2}{4D^{\#}\frac{x-x_1}{Y_{Cmax}}} \right) + \exp\left(-\frac{\left(\frac{y}{Y_{Cmax}} + 1\right)^2}{4D^{\#}\frac{x-x_1}{Y_{Cmax}}} \right) \right] \quad (4)$$

where Q_{air} is the air flux, Q is the water discharge, Y_{Cmax} is the transverse location where $C = C_{max,}$ x and y are directions along and normal to the flow, and $D^{\#}$ is a dimensionless diffusivity defined as $D\# = D_t/(V_1 d_1)$, with D_t the turbulent diffusivity in y-direction. Equation (4) is compared to experimental data in Fig. 6, where $D^{\#}$, C_{max} and Y_{max} were selected to best fit the data (Fig. 6, Red data).

In the hydraulic jump, the void fraction distributions presented a similar shape in the turbulent shear region. The void fraction data showed a local minimum C* at a characteristic elevation y*, corresponding to a transition between the turbulent shear region and the recirculation region above. In the upper flow region, the void fraction increased rapidly towards unity (Fig. 6), and followed a Gaussian error function [8]:

$$C = \frac{1}{2}\left[1 + \text{erf}\left(\frac{y - Y_{50}}{2\sqrt{\frac{D^* (x-x_1)}{V_1}}} \right) \right] \quad \text{for } y > y^* \quad (5)$$

where Y_{50} is the location where $C = 0.50$, and D* is a dimensionless diffusivity in the recirculation region. The experimental data are compared with the theoretical solutions for the turbulent shear layer ($y < y^*$, Eq. (4)) and the recirculation region ($y > y^*$, Eq. (5)) in Fig. 6.

A systematic comparison between plunging jet and hydraulic jump void fraction data was conducted for identical inflow conditions and at identical locations from the air entrapment. Close to the impingement perimeter, the void fraction distributions in plunging jet and hydraulic jump were typically similar, although the hydraulic jump data presented more scatter, and the void fractions in the plunging jet were slightly higher than in the hydraulic jump for $y < Y_{Cmax}$ (e.g. Fig. 6a). Further downstream, the data were generally close in the shear region, and markedly different in the outer flow region (i.e. recirculation). Overall, the void fractions in the turbulent shear layer followed quasi-Gaussian distributions in both plunging jet and hydraulic jump. Maxima in void fractions decreased with increasing distance from impingement (Appendix A), while the corresponding elevation increased, as shown in Fig. 7a, b respectively. Figure 7 shows the variation of C_{max} and Y_{Cmax} with increasing distance from the impingement point $(x-x_1)/d_1$.

The turbulent air-bubble diffusivity $D^{\#}$ reflected the strength of the turbulent advection process in the turbulent shear layer, while D* characterised the aeration and de-aeration process in the upper flow region. The diffusion coefficients $D^{\#}$ results for plunging jet and hydraulic jump are compared to the literature in Fig. 8a, b respectively. In the plunging jet, $D^{\#}$ ranged from 0.0053 to 0.019, and between 0.017 and 0.045 in the hydraulic jump. In comparison, D* was between 0.00012 and 0.024 in the recirculation. The data indicated that $D^{\#}$ remained approximately constant independently of the longitudinal distance from impingement, while D* tended to decrease with increasing the longitudinal distance from impingement.

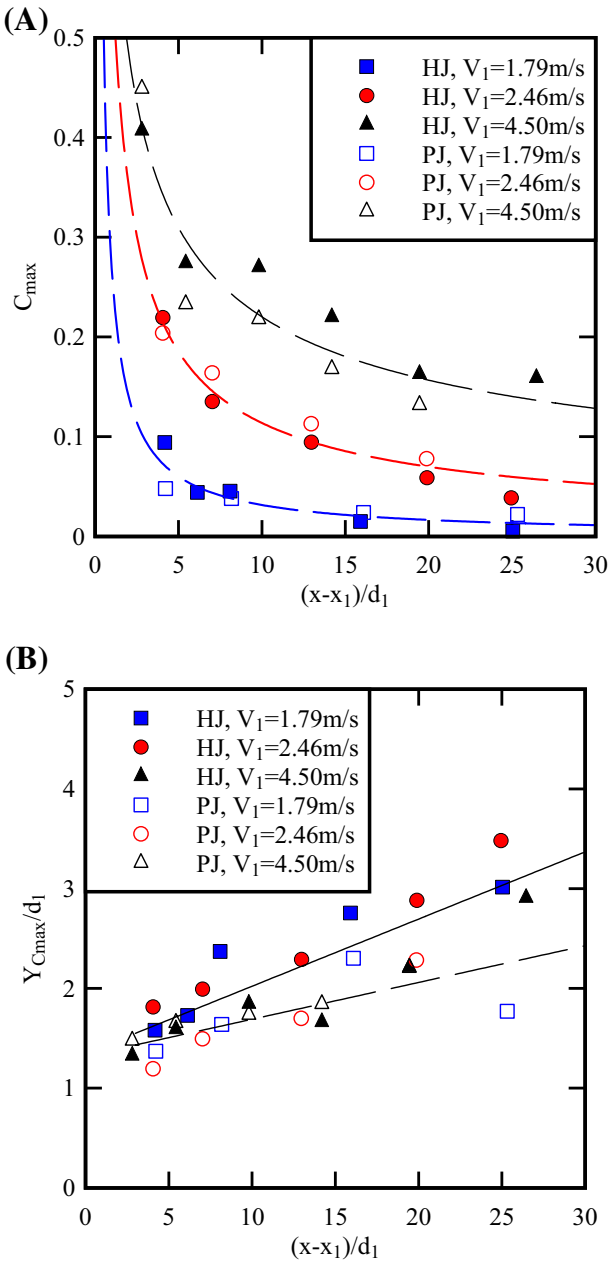

Fig. 7 Longitudinal distributions of maximum void fraction in shear layer C_{max} and its vertical elevation Y_{Cmax}/d_1 in the vertical plunging jet and horizontal hydraulic jump, **a** maximum void fraction in shear layer C_{max} with trend lines for each inflow velocity, **b** vertical elevation Y_{Cmax}/d_1—Comparison with Eq. (8a) for plunging jet (dashed line) and Eq. (8b) for hydraulic jump (solid line)

The bubble count rate profiles in plunging jet and hydraulic jump showed very similar trends, with a monotonic increase up to a maximum bubble count rate F_{max} and followed by a decrease towards zero, with increasing distance y from the support (Fig. 9). Further the maximum bubble count rate decreased with increasing distance from the impingement perimeter.

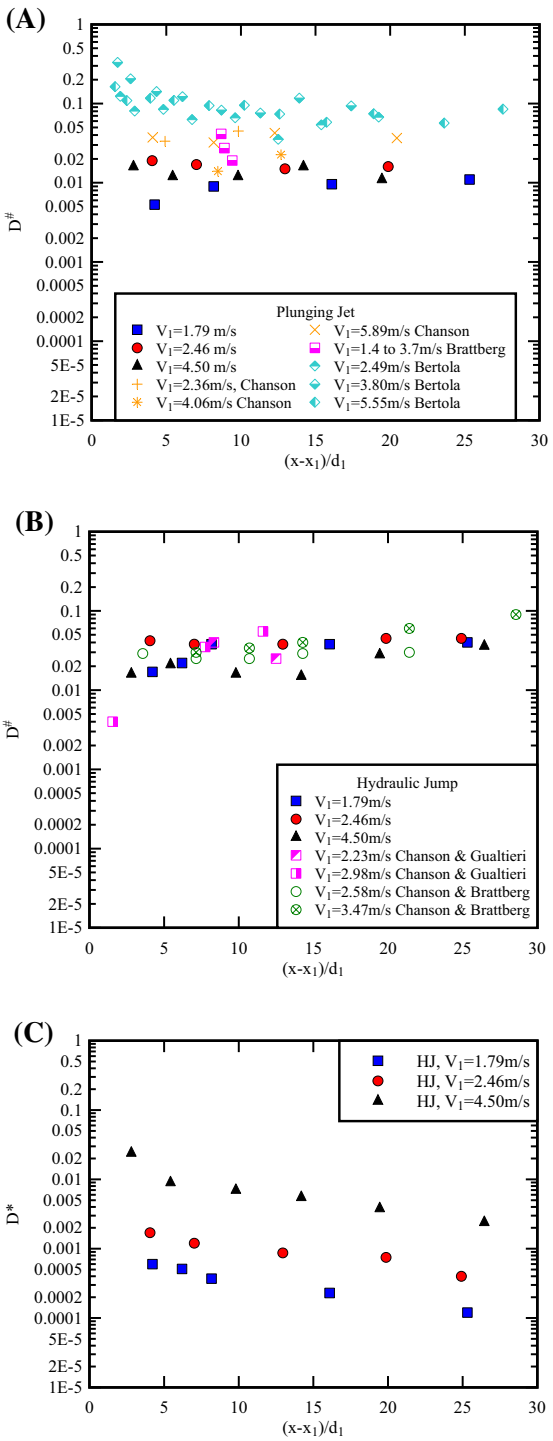

Fig. 8 Longitudinal variation of dimensionless diffusivities in the turbulent shear layer for hydraulic jump and plunging jet, and in the recirculation region of hydraulic jump, **a** Dimensionless diffusivity $D^{\#}$ in the turbulent shear layer of vertical plunging jet—Comparison with the data of [2, 5, 7], **b** Dimensionless diffusivity $D^{\#}$ in the turbulent shear layer of horizontal hydraulic jump—comparison with the data of [12, 13], **c** Dimensionless diffusivity D^{*} in the recirculation region of the hydraulic jump

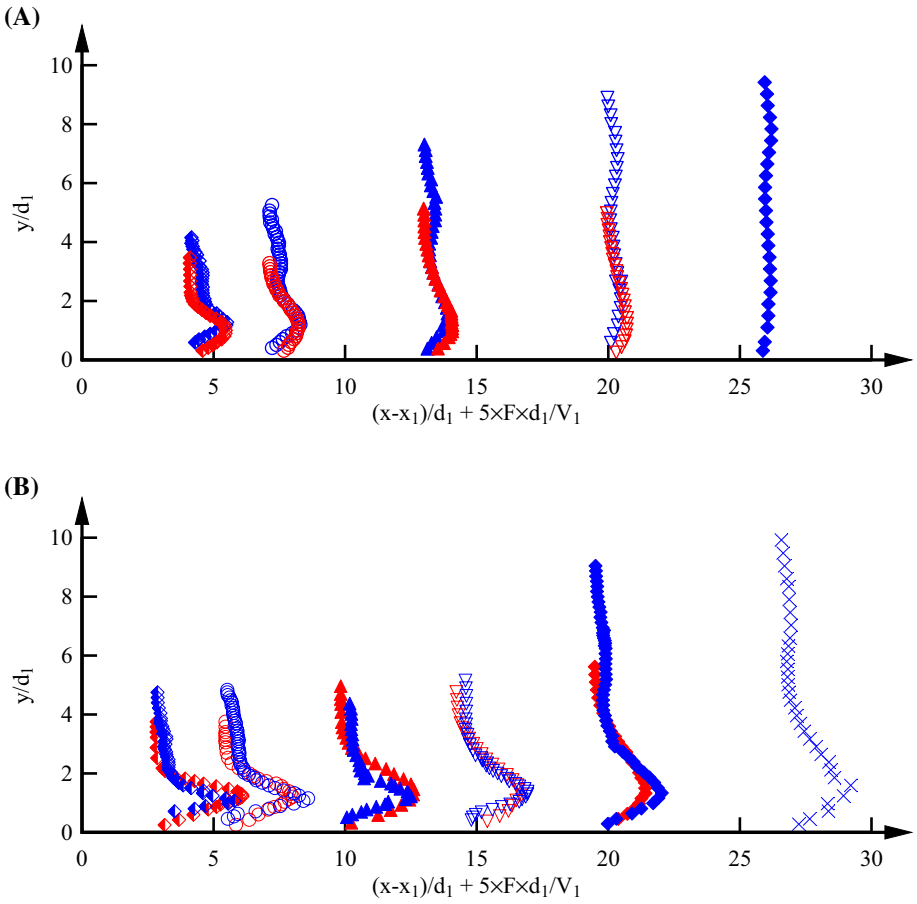

Fig. 9 Comparison in terms of bubble count rate distributions in vertical plunging jet (Red data) and horizontal hydraulic jump (Blue data) for two inflow velocities, **a** $V_1 = 2.46$ m/s, **b** $V_1 = 4.50$ m/s

Both the maximum bubble rate and its characteristic elevation were very close for both plunging jet and hydraulic jump, for a given inflow velocity and distance from impingement.

4.2 Interfacial velocity distributions

The interfacial velocity fields exhibited some characteristic distribution close to developing shear layer results. In the plunging jet, the velocity field was characterised by a positive velocity in the turbulent shear layer and a negative velocity in the upward flow region (Fig. 10a). The maximum velocity was close to the jet support. The velocity measurements compared well to a modified analytical solution of the equation of motion in a free shear layer:

$$\frac{V - V_{recirc}}{V_{max} - V_{recirc}} = \frac{1}{2}\left(1 - \text{erf}\left(K\frac{y - Y_{0.5}}{x - x_1}\right)\right) \quad (6)$$

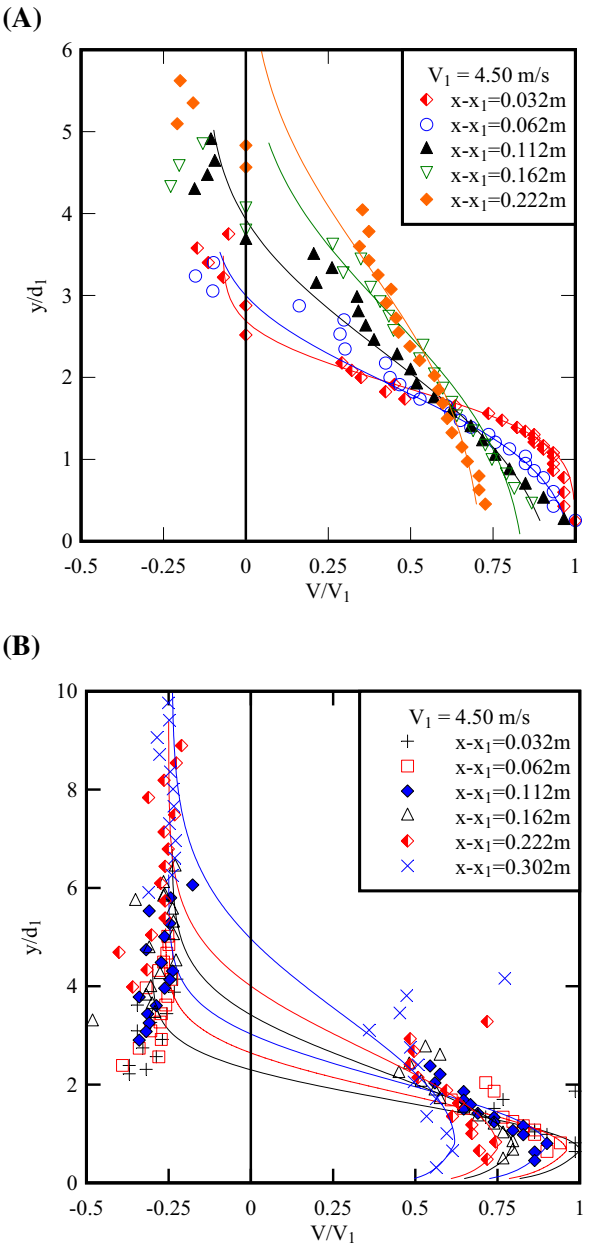

Fig. 10 Dimensionless vertical velocity profiles in vertical plunging jet and horizontal hydraulic jump for $V_1 = 4.50$ m/s, **a** Plunging jet data—Comparison with Eq. (6), **b** Hydraulic jump data—Comparison with Eq. (7)

where V is the time-averaged velocity, V_{recirc} is the mean recirculation velocity, V_{max} is the maximum velocity, $Y_{0.5}$ is the transverse position where $V = V_{max}/2$, and K is a coefficient inversely proportional to the momentum exchange coefficient ν_T, assumed constant across the shear layer: $\nu_T = V_1(x-x_1)(4K^2)$ [28]. Herein both V_{recirc} and K were deduced from the best data fit.

In the hydraulic jump, the velocity field showed a wall jet profile, with a markedly negative velocity in the recirculation region (Fig. 10b). The velocity profiles were self-similar:

$$\frac{V}{V_{max}} = \left(\frac{y}{Y_{Vmax}}\right)^{1/N} \quad \text{for } y < Y_{Vmax} \tag{7a}$$

$$\frac{V - V_{recirc}}{V_{max} - V_{recirc}} = \exp\left[-\frac{1}{2}\left(1.765\ \frac{y - Y_{Vmax}}{Y_{0.5}}\right)^2\right] \quad \text{for } y > Y_{Vmax} \tag{7b}$$

where Y_{Vmax} is the transverse position where $V = V_{max}$ and N is a constant found to be between 6 and 10. Figure 10 shows typical velocity profiles obtained in the plunging jet and the hydraulic jump. The data are compared to Eq. (6) (Plunging jet) and Eq. (7) (Hydraulic jump), showing a good agreement overall between data and analytical solutions.

The velocity distributions yielded some differences between plunging jet and hydraulic jump. The velocity profiles in the plunging jet were somehow similar to a free shear flow, with a buoyancy driven upward movement of air bubbles in the outer region. The hydraulic jump data exhibited a marked wall jet similarity, with large negative velocities in the upper region of the roller. For all three inflow velocities, the velocity data in the turbulent shear region were more scattered in the hydraulic jump than in the plunging jet, with increased scatter when V/V_1 tended towards zero.

A comparison between the plunging jet and hydraulic jump data yielded maximum velocities V_{max} corresponding well between the two configurations for all three inflow velocities. The longitudinal decay in terms of V_{max}/V_1 was consistent the decrease of interfacial velocity with increasing distance from impingement along the jump roller and in the plunge pool respectively. A comparison with previous data [2, 12] showed a good agreement (data not shown).

In the plunging jet, the momentum exchange coefficient ν_T was estimated based upon the best fit of the interfacial velocity data. For the hydraulic jump data, the eddy viscosity was assumed to be comparable to that of monophase wall jet flow [29]. The ratio of the air bubble turbulent diffusivity D_t to the eddy viscosity ν_T was deduced, providing a comparison in terms of differences between air diffusion and momentum diffusion. Experimental data are plotted as a function of the longitudinal position in Fig. 11. The results implied on average $D_t/\nu_T \sim 0.76$ in the hydraulic jump and $D_t/\nu_T \sim 0.24$ in the plunging jet. The main trend, i.e. $D_t/\nu_T \propto 10^0$, suggested that the air diffusion process is of the same order of magnitude, albeit lesser than the momentum exchange process in vertical and horizontal plunging jet flows, within the experimental flow conditions. With $D_t/\nu_T < 1$, the diffusion of vorticity was more important than the advective diffusion of air bubbles. The median value for the vertical plunging jet was smaller than the horizontal hydraulic jump results. The trend might suggest that the momentum transfer in the plunging jet might to be little affected by the advective diffusion process. Whereas the turbulent momentum transfer in the hydraulic jump seemed to reach the same order of magnitude than the advective diffusion process.

4.3 Air flux

Based upon the void fraction and velocity data, the air flux per unit width was calculated based upon the conservation of mass of the air phase:

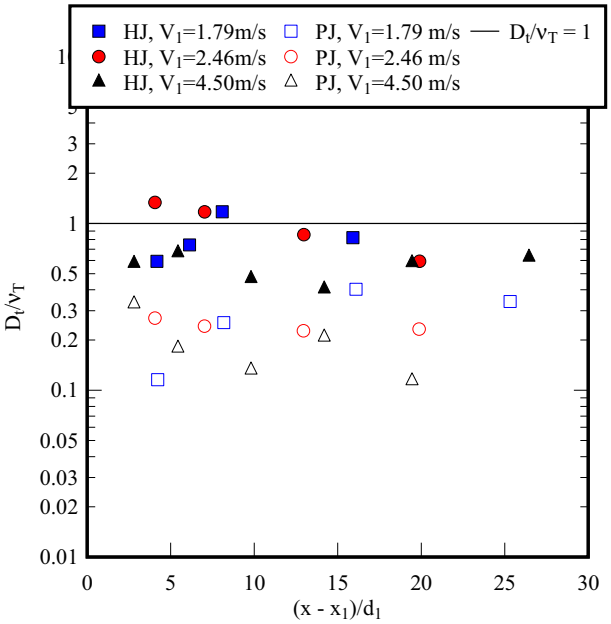

Fig. 11 Ratio of turbulent diffusivity to the eddy viscosity D_t/ν_T as a function of the longitudinal distance from the impingement point $(x\text{-}x_1)/d_1$ in vertical plunging jet and horizontal hydraulic jump

$$q_{air} = \int_{0}^{y(V=0)} C\,V\,dy \quad \text{for } V > 0 \tag{8}$$

$$q_{recirc} = \int_{y(V=0)}^{Y} C\,V\,dy \quad \text{for } V < 0 \tag{9}$$

where q_{air} is the positive air flux in the air-bubble diffusion layer and q_{recirc} is the negative air flux in the recirculation region (HJ) and the outer flow region (PJ) respectively. In the plunging jet, Y designated the transverse position where last data points were available and where C tended towards zero. In the hydraulic jump, Y was equal to Y_{90}, commonly accepted as an upper limit for the equivalent clear water depth [9].

Results for the entrained air flux q_{air} are presented in Fig. 12. The data showed that the dimensionless air fluxes q_{air}/q_w in plunging jet and hydraulic jump increased with increasing inflow velocity and decreased with increasing longitudinal distance from the impingement point for a given inflow velocity. The experimental data were close for both plunging jet and hydraulic jumps:

$$\frac{q_{air}}{q_w} = 4.03 \times 10^{-4} \left(\rho \frac{(V_1 - 1.76)\,d_1}{\mu}\right)^{0.49} \left(\frac{x - x_1}{d_1}\right)^{1.25 + \frac{68.4}{V_1^{8.64}}} \quad \text{for PJ and HJ data} \tag{10}$$

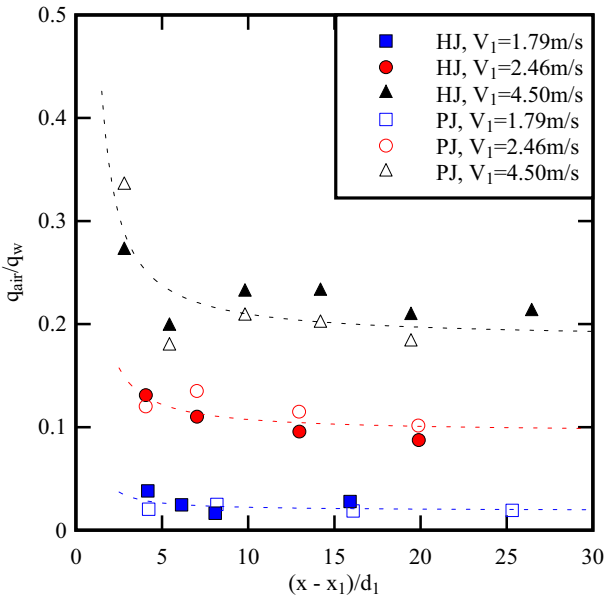

Fig. 12 Dimensionless flux q_{air}/q_w of entrained air as a function of the longitudinal distance from the impingement point for vertical plunging jet and horizontal hydraulic jump—Comparison with trend lines for each inflow velocity (Eq. 10)

with q_w the water flow per unit width., as shown in Fig. 12. The dimensionless recirculation air fluxes q_{recirc}/q_w in the hydraulic jump were best fitted by:

$$\frac{q_{recirc}}{q_w} = -0.53\ e^{-\frac{2.24\ d_1}{x-x_1}} \quad \text{for HJ data} \tag{11}$$

The recirculation air fluxes in the plunging jet were significantly smaller than in the hydraulic jump: $q_{recirc}/q_w \sim 0$ to 1.4×10^{-4}, and sometimes no recirculation motion could be detected.

4.4 Turbulence intensity

The turbulence intensity is defined herein as the ratio of the root mean square velocity fluctuation v' to the inflow V_1, and calculated based on the cross-correlation and auto-correlation data (Appendix B). Typical results are shown in Fig. 13, for an inflow velocity $V_1 = 1.79$ m/s.

The plunging jet data distributions showed relatively constant turbulence intensities across the shear layer, with a greater data scatter away from the support. In the hydraulic jump, however, turbulence intensities were comparable to the plunging jet data at locations close to the channel bottom, increasing with increasing elevation, becoming highly scattered and reaching possibly-meaningless values for $y/d_1 > 1.5$. Such outliers were previously reported in hydraulic jumps [32], and believed to be related to the large-scale longitudinal fluctuating motions of the roller toe.

4.5 Particle chord length distributions and air–water specific interface area

The bubble chord lengths ch were derived from the bubble chord time measurements:

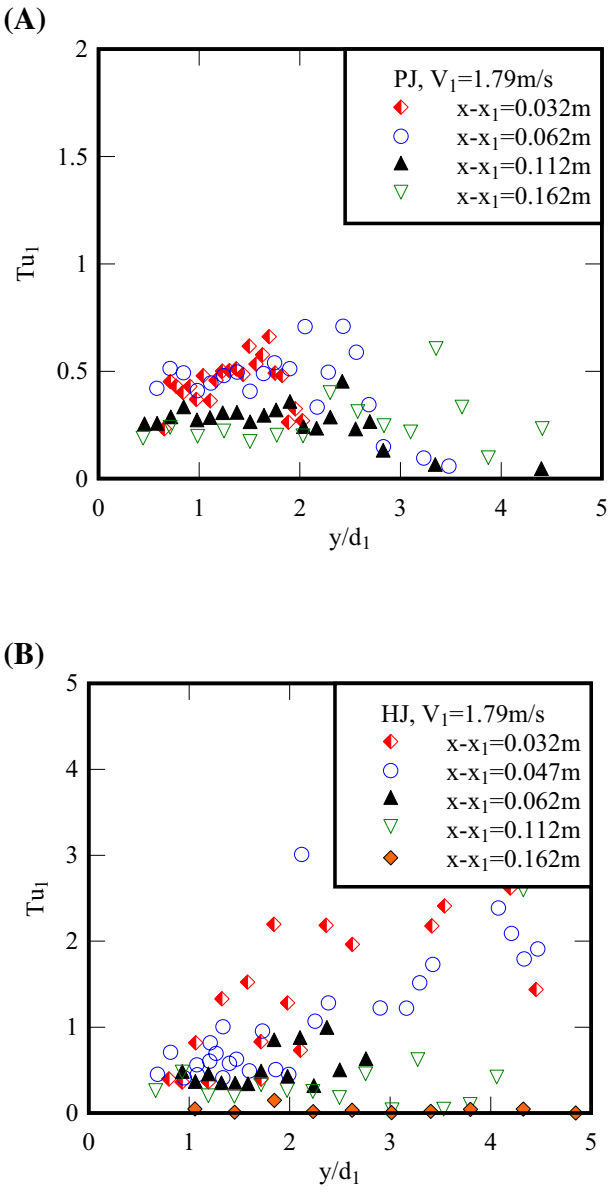

Fig. 13 Longitudinal variation of turbulence intensity $Tu_1 = u'/V_1$ in the vertical plunging jet and horizontal hydraulic jump for $V_1 = 1.79$ m/s, **a** Plunging jet, **b** Hydraulic jump

$$ch = Vt_{ch} \tag{12}$$

where t_{ch} is the chord time and V the time-averaged interfacial velocity. For each cross-section, the bubble chord size distributions were plotted at three characteristic locations: i.e. at Y_{Cmax} where $C = C_{max}$, at Y_{Fmax} where $F = F_{max}$ for both plunging jet and hydraulic jump, and at $Y_{0.5}$ where $V = V_{max}/2$, for the plunging jet and at Y_{Vmax} where $V = V_{max,}$ for the hydraulic jump. Typical results are presented in Fig. 14, where the figure caption gives the values of maximum void fractions, maximum bubble count rates and dimensionless

	Plunging Jet			Hydraulic Jump		
$(x - x_1)/d_1$ (m)	C_{max}	F_{max} (Hz)	$V_{max}/(2\ V_1)$	C_{max}	F_{max} (Hz)	V_{max}/V_1
0.062	0.233	203.7	0.500	0.274	249.1	0.905
0.222	0.168	197.2	0.434	0.163	203.9	0.715

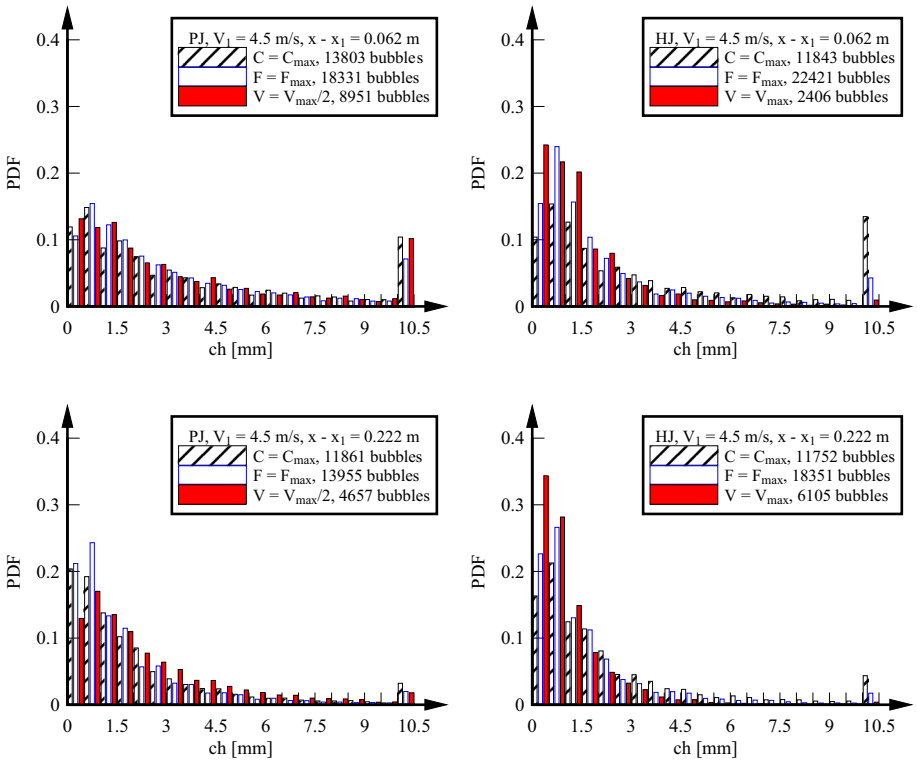

Fig. 14 Probability density functions (PDFs) of bubble chord lengths ch (mm) at characteristic locations for plunging jet (Left) and hydraulic jump (Right) at $x - x_1 = 0.062$ and 0.222 m—Data for ch = 10.5 mm corresponds to chord lengths ≥ 10 mm—Flow conditions: $V_1 = 4.50$ m/s, $Fr_1 = 13.5$, $Re_1 = 5.14 \times 10^4$

maximum interfacial velocities. In Fig. 14, each column corresponds to the probability of bubble chord lengths in intervals of 0.5 mm. For instance, the column ch = 3 mm corresponds to the probability of chord lengths between 3 and 3.5 mm. The data for the last column give the probability of ch ≥ 10 mm.

Overall the data showed generally a similar trend for all inflow velocities. The distributions of bubble chords were positively skewed, with the mode having a size less than 1.5 mm. Close to impingement, the data showed a larger fraction of large bubbles. With increasing distance from the impingement, the probability density functions shifted towards smaller bubbles, e.g. the probability of smaller bubbles increased whereas the probability of bubble chords larger than 10 mm decreased. The findings suggested the entrapment of large air packets at impingements, which would be broken-up as they were advected downstream within the turbulent shear layer [7, 9].

The bubble chord mean data showed an overall decrease in mean bubble chord length with increasing distance from the impingement point and with decreasing inflow velocity (Fig. 15a). Since the bubble chord PDFs were skewed, the skewness and the kurtosis data are also shown in Fig. 15 for completeness. The hydraulic jump data showed a higher skewness and kurtosis, compared to the plunging jet results. This finding indicated a higher amount of large bubbles (2 mm < ch < 10 mm) in the plunging jet compared to the hydraulic jump. In addition, the hydraulic jump data exhibited an important proportion of very large bubbles (ch > 10 mm). Effectively, the bubble chord lengths in the hydraulic jump were mainly concentrated to sizes between 0 and 1.5 mm. The plunging jet data showed a broader range of entrained bubble sizes, with relatively high probabilities for ch > 2 mm, especially for cross-sections close to impingement.

The specific air–water interface area a is defined as the ratio of the air–water interface area to the total volume of air and water. It was estimated as:

$$a = \frac{4F}{V} \tag{13}$$

where F is the bubble count rate and V is the interfacial velocity [10]. Equation (13) is only valid in the bubbly flow, for regions with void fractions lower than 30%. Figure 16 shows the specific air–water interface area as a function of $(x-x_1)/d_1$ at the characteristic location where $F=F_{max}$. For the two lower inflow velocities, the specific interface area a decreased with increasing longitudinal distance from the impingement point. For $V_1=4.50$ m/s, the data were more scattered. Altogether, all the data showed that the specific air–water interface area increased with increasing inflow velocity.

5 Conclusion

This study presents a systematic quantitative comparison of the similarities and differences between horizontal (hydraulic jump) and vertical supported jets (plunging jet). The work was undertaken through detailed physical experiments carried out under identical inflow conditions in terms of inflow length, inflow depth and inflow velocity, as well as using the same instrumentation. Video analyses of the impingement perimeter yielded substantial differences in terms of the impingement conditions between the two configurations. Larger maximum amplitudes of the impingement perimeter fluctuations were observed in the hydraulic jump, combined with impingement perimeter fluctuation frequencies independent of the inflow velocity. In the plunging jet, frequencies increased with decreasing inflow velocity.

Phase-detection probe measurements allowed the systematic characterisation of a broad range of multiphase flow parameters, including the interfacial velocity, void fraction, bubble count rate and bubble chord size for three impact velocities $V_1 = 1.79$ m/s, 2.46 m/s and 4.50 m/s. Similarities were observed in terms of local air entrainment at the impingement point, void fraction distributions and dimensionless turbulent diffusivities. Void fractions in the turbulent shear layer followed a quasi-Gaussian distribution in both plunging jet and hydraulic jump. Maximum void fractions decreased and void fraction distributions widened with increasing distance from the impingement point, indicating an advective diffusion process of air bubbles Smoother distributions were found in the plunging jet, whereas the hydraulic jump data were more scattered at cross-sections close to impingement, because of the streamwise fluctuations of the

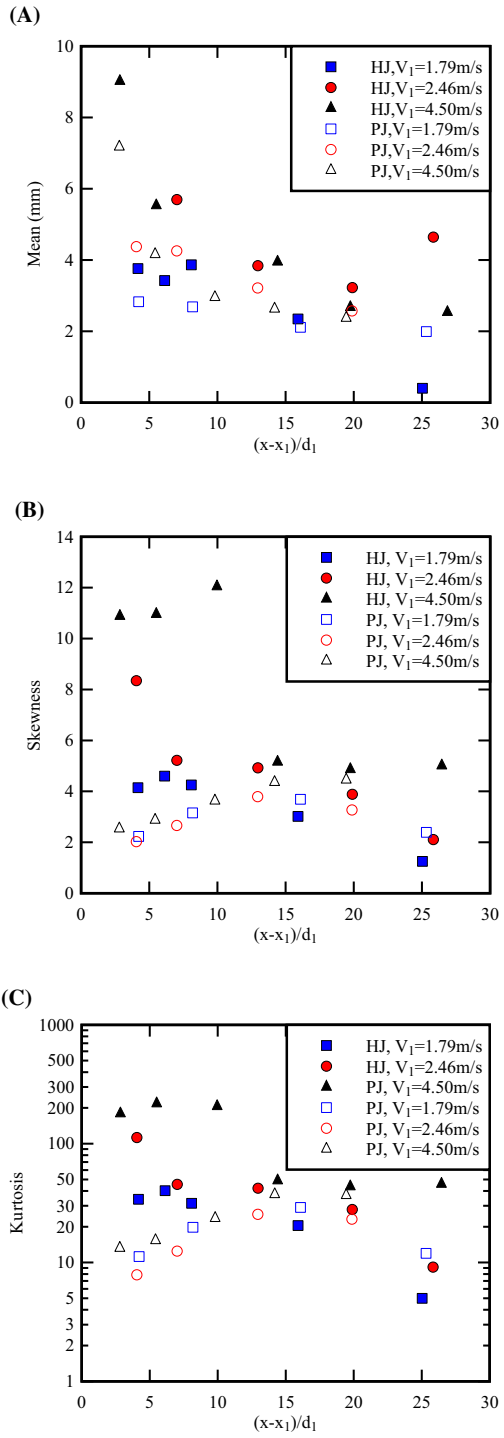

Fig. 15 Mean, skewness and kurtosis of bubble chord length ch (mm) in vertical plunging jet and horizontal hydraulic jump as functions of the longitudinal distance from the impingement point, **a** Mean bubble chord length, **b** Skewness, **c** Kurtosis

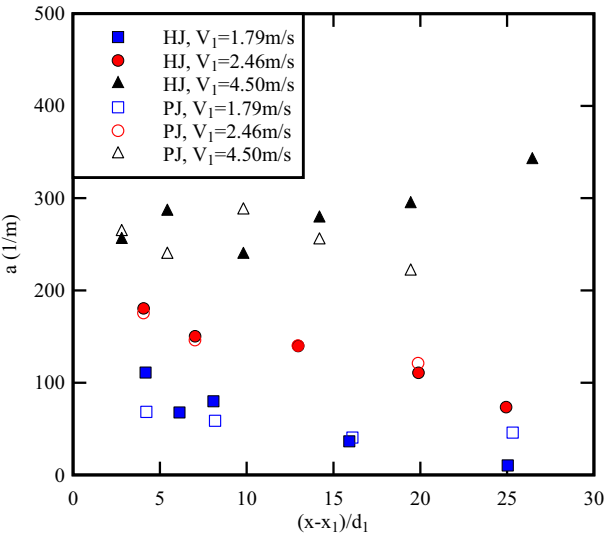

Fig. 16 Specific air–water interface area as a function of the longitudinal distance from the impingement point at the characteristic location $F = F_{max}$

jump toe. The turbulent diffusivities were approximately constant over the longitudinal distance from the impingement point independently of the velocity and the setup.

Although both configurations are seminal examples of local air entrainment and the hydraulic jump was described as a limiting case of a horizontal plunging jet, some differences were shown, mainly regarding the velocity distributions, the direction of buoyancy force and the interfacial aeration in the hydraulic jump. The velocity distributions presented substantial differences in the outer region: the hydraulic jump velocity data exhibited an important negative velocity in the recirculation region, following closely a wall jet solution, whereas the velocity profiles in the plunging jet were close to a free shear flow, with some buoyancy driven upward movement of air bubbles away from the support. Some substantial aeration and de-aeration took place at the free surface in the hydraulic jump roller. The different velocity profiles as well as the interfacial aeration in the upper recirculation underlined differences between plunging jet and hydraulic jump in terms of both the momentum transfer process and the air diffusion process.

Further research is recommended at higher Reynolds numbers, for hydraulic and fluvial applications. A systematic comparison with inclined jets would add valuable information. Different instrumentation, e.g. with very small probe tip diameters, could yield additional information concerning the microscopic structure of the flow. Additionally, oxygen measurements of the oxygen content in the flow upstream and downstream of the impingement point would add information on the oxygenation power of both plunging jets and hydraulic jumps.

Acknowledgements The authors thank Dr Hang Wang (Sichuan University), Dr Matthias Kramer (The University of Queensland) and Dr Xinqian (Sophia) Leng (The University of Queensland) for helpful discussions. They further acknowledge the technical assistance of Jason Van Der Gevel and Stewart Matthews (The University of Queensland).

Appendix A: Maximum void fraction in the shear layer

In the developing shear layer, the void fraction data followed a quasi-Gaussian distribution in both plunging jet and hydraulic jump. Maxima in void fractions decreased with increasing distance from impingement, while the corresponding elevation increased, as shown in Fig. 7 presenting the variation of C_{max} and Y_{Cmax} with increasing distance from the impingement point $(x-x_1)/d_1$. The decay in maximum void fraction was best fitted with a power law decay function:

$$C_{max} = A \left(\frac{x - x_1}{d_1} \right)^B \tag{14}$$

where the coefficients A and B are summarised in Table 3. Equation (14) is compared to experimental data in Fig. 7a. The observations showed a linear increase of the characteristic location Y_{Cmax} with increasing distance from the impingement point, in both plunging jet and hydraulic jump. Figure 7b shows linear trend lines for plunging jet data (dashed line) and hydraulic jump data (solid line). The slope of the hydraulic jump trend line was almost double the slope from the plunging jet trend line:

$$\frac{Y_{Cmax}}{d_1} = 1.32 + 0.037 \left(\frac{x - x_1}{d_1} \right) \quad \text{for plunging jet data} \tag{15}$$

$$\frac{Y_{Cmax}}{d_1} = 1.35 + 0.067 \left(\frac{x - x_1}{d_1} \right) \quad \text{for hydraulic jump data} \tag{16}$$

Appendix B: Turbulence intensity in air–water flows

When the velocity is measured with a dual-tip probe, the dimensionless standard deviation of the interfacial velocity V equals:

$$Tu = \frac{v'}{V} = \frac{\sqrt{\sigma_{xy}^2 - \sigma_{xx}^2}}{T} \tag{17}$$

where σ_{xy} is the standard deviation of the cross-correlation function, σ_{xx} is the standard deviation of the autocorrelation function, and T is the travel time for which the cross-correlation function is maximum. Kipphan [22] developed a similar result for two-phase mixtures in pneumatic conveying.

Table 3 Coefficients of the power law decay of maximum void fraction in the shear layer of vertical plunging jet and horizontal hydraulic jump

V_1 (m/s)	A	B
1.79	0.268	−0.930
2.46	0.575	−0.704
4.50	0.682	−0.491

Assuming that the successive detections of bubble interfaces by the probe sensors is a true random process, the cross-correlation function is a Gaussian distribution, and Eq. (17) becomes:

$$\mathrm{Tu} = \frac{\sqrt{2}}{\sqrt{\pi} \times \mathrm{T}} \times \sqrt{\left(\frac{\mathrm{T_{xy}}}{(\mathrm{R_{xy}})_{\max}}\right)^2 - \mathrm{T_{xx}^2}} \tag{18}$$

where T_{xy} is the cross-correlation integral time scale, T_{xx} is the auto-correlation time scale, and $(R_{xy})_{max}$ is the maximum cross-correlation (when the time lag equals T) [18].

Assuming that the cross-correlation function is a Gaussian distribution and defining $\tau_{0.5}$ the time scale for which: $R_{xy}(T+\tau_{0.5}) = R_{xy}(T)/2$, and $T_{0.5}$ is the characteristic time for which the normalised auto-correlation function equals 0.5, Eq. (23) yields:

$$\frac{\mathrm{v'}}{\mathrm{V}} = 0.851 \times \frac{\sqrt{\tau_{0.5}^2 - \mathrm{T_{0.5}^2}}}{\mathrm{T}} \tag{19}$$

Note that the calculations become indeterminate when the time-averaged velocity V tends to zero.

References

1. Bakhmeteff BA, Matzke AE (1936) The hydraulic jump in terms of dynamic similarity. Trans ASCE 101:630–647 **(Discussion: Vol. 101, pp. 648-680)**
2. Bertola N, Wang H, Chanson H (2018) A physical study of air-water flow in planar plunging water jets with large inflow disturbance. Int J Multiphase Flow 100:155–171. https://doi.org/10.1016/j.ijmultiphaseflow.2017.12.01
3. Bertola NJ, Wang H, Chanson H (2018) Air bubble entrainment, breakup and interplay in vertical plunging jets. J Fluids Eng. https://doi.org/10.1115/1.4039715
4. Bin A (1993) Gas entrainment by plunging liquid jets. Chem Eng Sci 48(2):3585–3630
5. Brattberg T, Chanson H (1998) Air entrapment and air bubble dispersion at two-dimensional plunging water jets. Chem Eng Sci 53(24):4113–4127. https://doi.org/10.1016/s0009-2509(98)80004-3
6. Brown GL, Roshko A (1974) On the density effects and large structure in turbulent mixing layers. J Fluid Mech 64:775–816
7. Chanson H (1995) Air entrainment in two-dimensional turbulent shear flows with partially developed inflow conditions. Int J Multiphase Flow 21(6):1107–1121. https://doi.org/10.1016/0301-9322(95)00048-3
8. Chanson H (1996) Air bubble entrainment in turbulent water jets discharging into the atmosphere. Aust Civil Eng Trans. 39(1):39–48
9. Chanson H (1997) Air bubble entrainment in free-surface turbulent shear flows. Academic Press, London, (ISBN 0-12-168110-6)
10. Chanson H (2002) Air-water flow measurements with intrusive phase-detection probes. Can we improve their interpretation? J Hydraul Eng 128(3):252–255. https://doi.org/10.1061/(ASCE)0733-9429(2002)128:3(252)
11. Chanson H (2010) Convective transport of air bubbles in strong hydraulic jumps. Int J Multiphase Flow 36(10):798–814. https://doi.org/10.1016/j.ijmultiphaseflow.2010.05.006
12. Chanson H, Brattberg T (2000) Experimental study of the air-water shear flow in a hydraulic jump. Int J Multiphase Flow 26(4):583–607. https://doi.org/10.1016/S0301-9322(99)00016-6
13. Chanson H, Gualtieri C (2008) Similitude and scale effects of air entrainment in hydraulic jumps. J Hydraul Res 46(1):35–44
14. Cummings PD, Chanson H (1997) Air entrainment in the developing flow region of plunging jets. Part 1: theoretical development. J Fluids Eng 119(3):597–602. https://doi.org/10.1115/1.2819286
15. Cummings PD, Chanson H (1997) Air entrainment in the developing flow region of plunging jets. Part 2: experimental. J Fluids Eng 119(3):603–608. https://doi.org/10.1115/1.2819287

16. Ervine DA (1998) Air entrainment in hydraulic structures: a review. In: Proceedings of the institution of civil engineers: water and maritime engineering, UK, vol 130, pp 142–153
17. Ervine DA, McKeogh EJ, Elsawy EM (1980) Effect of turbulence intensity on the rate of air entrainment by plunging water jets. In: Proceedings of the institution of civil engineers, Part 2, June, pp 425–445
18. Felder S, Chanson H (2014) Triple decomposition technique in air-water flows: application to instationary flows on a stepped spillway. Int J Multiph Flow 58:139–153. https://doi.org/10.1016/j.ijmultiphaseflow.2013.09.006
19. Foglizzo T, Masset F, Guilet J, Durand G (2012) Shallow water analogue of the standing accretion shock instability: experimental demonstration and a two-dimensional model. Phys Rev Lett 108(5):051103
20. Goldring BT, Mawer WT, Thomas N (1980) Level surges in the circulating water downshaft of large generating stations. In: Proceedings of 3rd international conference on pressure surges, BHRA Fluid Engineering, F2, Canterbury, UK, pp 279–300
21. Henderson FM (1966) Open channel flow. MacMillan Company, New York
22. Kipphan H (1977) Bestimmung von Transportkenngrößen bei Mehrphasenströmungen mit Hilfe der Korrelationsmeßtechnik. Chem Ing Tec 49(9):695–707 **(in German)**
23. Koochesfahani MM, Dimotakis PE (1985) Laser-induced fluorescence measurements of mixed fluid concentration in a liquid plane shear layer. AIAA J 23(11):1700–1701
24. Murzyn F, Mouaze D, Chaplin JR (2005) Optical fibre probe measurements of bubbly flow in hydraulic jumps. Int J Multiphase Flow 31(1):141–154
25. Rajaratnam N (1962) An experimental study of air entrainment characteristics of the hydraulic jump. J Inst Eng India 42(7):247–273
26. Rajaratnam N (1965) The hydraulic jump as a wall jet. Jl of Hyd. Div., ASCE, vol 91, No. HY5, pp 107-132. Discussion : vol 92, No. HY3, pp 110-123 & vol 93, No. HY1, pp 74-76
27. Rao NSL, Kobus HE (1974) Characteristics of self-aerated free-surface flows. In: Water and waste water/current research and practice, vol 10, Eric Schmidt Verlag, Berlin, Germany
28. Schlichting H (1979) Boundary layer theory. McGraw-Hill, New York, USA, 7th edition
29. Schwarz WH, Cosart WP (1961) The two-dimensional wall-jet. J Fluid Mech 10(4):481–495
30. Sene KJ, Thomas NH, Goldring BT (1989) Planar plunge-zone flow patterns and entrained bubble transport. J Hydraul Res 27(2):363–383
31. Sene KJ, Hunt JCR, Thomas NH (1994) The role of coherent structures in bubble transport by turbulent shear flows. J Fluid Mech 259:219–240
32. Wang H (2014) Turbulence and air entrainment in hydraulic jumps. Ph.D. thesis, School of Civil Engineering, The University of Queensland, Brisbane, Australia, 341 pages & Digital appendices (https://doi.org/10.14264/uql.2014.542)
33. Wang H, Chanson H (2015) Air entrainment and turbulent fluctuations in hydraulic jumps. Urban Water J 12(6):502–518. https://doi.org/10.1080/1573062X.2013.847464
34. Wood IR (1991) Air entrainment in free-surface flows. IAHR Hydraulic structures design manual No.4, Hydraulic design considerations, Balkema Publ., Rotterdam, The Netherlands, 149 pages, (ISBN 978-90-6191-994-0)
35. Zhang G, Wang H, Chanson H (2013) Turbulence and aeration in hydraulic jumps: free-surface fluctuation and integral turbulent scale measurements. Environ Fluid Mech 13(2):189–204. https://doi.org/10.1007/s10652-012-9254-3

Publisher's Note Springer Nature remains neutral with regard to jurisdictional claims in published maps and institutional affiliations.